Beyond *N*-body: 3D cosmological gas dynamics

August E. Evrard *Institute of Astronomy, Madingley Road, Cambridge CB3 0HA*

Summary. We present a numerical method for following the hydrodynamics of a gaseous component in 3D cosmological simulations containing both gas and collisionless components. The code is the merged product of two existing approaches – the high-resolution P3M *N*-body program developed by Efstathiou & Eastwood, and SPH, the smoothed particle hydrodynamics approach of Monaghan & Gingold. The gas physics incorporated within the model includes self-gravity, the gravity from additional collisionless components, adiabatic heating, heating due to shocks, and radiative cooling. The use of variable spatial resolution allows reliable definition of a wide dynamic range. This makes the code optimal for tackling the general problem of clustering from an initially Gaussian random field.

Tests of the method are presented, with emphasis on following the collapse and shock-heating of initially cold clouds. This is done both for self-gravitating evolution and for the case of a spherical rich cluster in an $\Omega = 1$ universe with 10 per cent gas and 90 per cent dark matter. Resolution limits for applications to the evolution of X-ray gas in rich clusters and to the galaxy formation problem are estimated to demonstrate that interesting problems can be tackled with even moderate micro-computing capacity.

1 Introduction

An important move forward in simulations of cosmological structure is the inclusion of the hydrodynamics and thermal history of a gaseous component. Solving the general 3D problem poses a formidable challenge to any hydrodynamic method. For example, in hierarchical clustering models, initial mass distributions sampled from Gaussian random fields will, for many interesting power spectra, lead to a high degree of substructure present at all stages of the evolution. Grid-based hydrodynamic techniques currently lack the resolution (in 3D) necessary to evolve several levels of a clustering hierarchy simultaneously. A particle-based method known as SPH [Smoothed Particle Hydrodynamics, Gingold & Monaghan (1977), Lucy (1977), Monaghan (1985)] appears best suited for cosmological application. In this paper, we present a method designed to follow the hydrodynamics of a gas in a multi-component system consisting of gas and one or more collisionless components (e.g. dark matter, galaxies). The scheme is

essentially a merger of SPH with the P3M *N*-body program of Efstathiou & Eastwood (1981), described in detail by Efstathiou *et al.* (1985).

Within the gravitational instability picture of structure formation, two important ingredients for successful application of the code are the ability to shock-heat initially cold gas and the ability for gas to cool dissipatively. After baryon–photon decoupling, primordial gas cools adiabatically to low temperatures while density perturbations grow in the linear regime. Eventually, perturbations larger than some cosmologically dependent Jeans mass will go non-linear. On collapse, the gas in these objects will be shock-heated to the appropriate virial temperature – the kinetic energy of infall being converted into heat. This hot plasma will be able to cool radiatively, and cooling is expected to be dynamically important on galactic and smaller scales, while for groups and clusters of galaxies, the cooling timescales are long compared to the Hubble time (Rees & Ostriker 1977; Silk 1977; White & Rees 1978; Blumenthal *et al.* 1984). The algorithm described here is capable of modelling both shock heating and radiative cooling in a 3D and self-consistent fashion. The tests presented below concentrate only on the shock-heating process, a detailed examination of cooling will be presented in a later paper.

SPH employs a set of particles to represent the distribution of gas. The particles are labelled with a local temperature or entropy, along with the usual kinematic information. Local densities are determined by an interpolation or smoothing of the nearby particle distribution. The smoothing scale governs the hydrodynamic resolution of the code. Allowing the smoothing length to vary both spatially and temporally greatly increases the method's useful dynamic range and optimizes the code's ability to tackle the general problem of clustering from an initially Gaussian random field.

Previous simulations of cosmological gas dynamics simplified the general 3D problem, either by imposing symmetry or by idealizing the gas interactions. For example, the symmetric appearance of rich galaxy clusters in both the optical and X-ray led some authors to pursue spherically symmetric models for the cluster evolution (Gull & Northover 1975; Lea 1976; Perrenod 1978). Problems arose in modelling the potential, to the extent that Lea (1976) found oscillations of the post-shock gas large enough to cause variations of up to three orders of magnitude in the X-ray luminosity while Perrenod (1978), employing an evolving rather than static potential, found the gas to evolve quasistatically in a slowly deepening potential. A further difficulty with 1D studies is the fact that although the spherical approximation may be valid for the final state, at earlier times the system is likely to have been highly inhomogeneous [*cf.* the evolution of galactic halos in the simulations of Frenk *et al.* (1985)]. This throws into question results of evolutionary models based on spherical symmetry throughout.

Simplified gas interactions were pioneered by Larson (1969), and similar methods have been used extensively by Carlberg (1984, 1988) and recently by Baron & White (1987). The idea is to mimic gas physics of interest by adding some simple rules for gas particle interactions. Generally, these interactions are based on nearest neighbour collisions, and empirically-fitted free parameters must be introduced to control the processes. Although these methods are extremely useful in giving qualitative insight into difficult physical situations, they suffer a fundamental difficulty in how to relate the adopted numerical procedure and its parameters to known physical processes.

Doing the hydrodynamics will, in principle, circumvent these difficulties, but not without introducing new problems to be overcome. For example, when thermal pressure is dynamically important, as in the post-shock regions of a collapsed cloud, it is important to demonstrate within the numerical model that the kinetic pressure of particles' random motions is small compared to the thermal pressure. Essentially, the condition $(\sigma/c)^2 \ll 1$, where σ is the local velocity dispersion and c the sound speed, should hold in order to avoid 'double-counting' of the pressure. Another important problem is to prevent excessive transport occurring during collisions of gas streams at high mach number. The molecular viscosity of real gas will efficiently translate a collision's kinetic

energy into heat and prevent bulk free-streaming. In the numerical models a suitable artificial viscosity, effective on roughly the mean free path of the simulated particles, is employed for this purpose.

The details of SPH gas dynamics and its imbedding within the P3M *N*-body framework is discussed in Section 2. In Section 3, several tests are presented, including static demonstrations of density and gradient measurement, self-similar adiabatic expansion, and results of shock-heating for both self-gravitating and dark-matter driven collapses. In Section 4, some resolution estimates for problems on galactic and galaxy cluster scales are presented. A short summary follows in Section 5.

2 P3MSPH

The method aims to follow the self-consistent evolution of two density fields, $\varrho_g(x)$ and $\varrho_d(x)$, representing gas and a collisionless component (assumed from here on to be dark matter) respectively. For the gas, a temperature or entropy field must be specified along with an equation of state $P=P(\varrho, T)$. The *N*-body approximation discretizes the above continuous fields into sets of particles so, for example, there will be n_g gas particle each of mass m_g and N_d dark each of mass m_d. Initially, all particles are tagged with kinematic information (positions and momenta). In addition, each gas particle is labelled with a local specific thermal energy

$$\epsilon=kT/(\gamma-1)\mu m_p. \tag{1}$$

Working in the comoving frame, $\mathbf{x}=\mathbf{r}/a$, where a is the scale factor, the gas elements follow the equations of motion

$$\frac{d\mathbf{x}}{dt}=\mathbf{v}, \tag{2a}$$

$$\frac{d\mathbf{v}}{dt}=-2H\mathbf{v}-\frac{1}{a^2}\frac{\nabla P}{\varrho}-\frac{1}{a^3}\nabla\tilde{\Phi}(x), \tag{2b}$$

$$\frac{d\epsilon}{dt}=\frac{P}{\varrho^2}\frac{d\varrho}{dt}-\frac{\varrho\Lambda(\epsilon)}{(\mu m_p)^2}. \tag{2c}$$

Here $\mathbf{v}$ is the peculiar velocity, $H=\dot{a}/a$ is the Hubble parameter, $\tilde{\Phi}(x)$ is the peculiar gravitational potential, and $\Lambda(\epsilon)$ is a radiative cooling function. The inclusion of other source or transport terms in the energy equation is possible. The equations of motion for the dark matter are given by equations (2a) and (2b) with $P=0$. Setting $a\equiv1$ recovers the equations of motion in a non-expanding frame. Energy conservation for a comoving volume is given by a version of the cosmic energy equation (see Peebles 1980, section 24) modified to take into account gas pressure and radiative losses.

2.1 COLLISIONLESS *N*-BODY CLUSTERING IN P3M

The P3M algorithm is an efficient, high resolution scheme for performing collisionless cosmological clustering simulations. It has been used to model structure in a variety of cosmogonic scenarios, most recently for a universe dominated by cold dark matter (Davis *et al.* 1985; Frenk *et al.* 1985, 1987). Detailed discussions of P3M can be found in Hockney & Eastwood (1981) and Efstathiou *et al.* (1985). Some relevant features of the code will be presented here.

The key ingredient which gives the scheme its high resolution is the splitting the gravitational

acceleration calculation into two components

$$g_i = g_i^{LR} + g_i^{SR}(r_c). \tag{3}$$

the long-range component g_i^{LR} is calculated by Fourier transform while $g_i^{SR}(r_c)$ is found by direct summation over neighbouring particles within a distance r_c of particle i. Typically, $r_c \approx 0.05 L$, where L is the length of the simulated cube. Linked lists provide an efficient means of locating nearby particles. Periodic boundary conditions are used in conjunction with the long-range FFT. The interpretation of the calculation is that one is simulating a representative region in an infinitely periodic universe.

A fixed timestep is employed in a straightforward, second order accurate leapfrog integrator. Positions and accelerations are centred on the timestep and velocities on the half-timestep. To avoid numerical instability and to prevent two-body encounters from driving the evolution of the system, the gravitational potential is softened

$$V(r) = -Gm/(r^2 + \varepsilon^2), \tag{4}$$

where the softening parameter ε is chosen as small as possible to achieve high resolution, but not so small as to violate either the numerical stability condition or the condition that the dynamics be controlled by mean field fluctuations. For a relaxed configuration of total mass M and size R composed of particles of mass m, the rough criterion $Gm/\varepsilon \ll GM/R$ should be satisfied for the system to be thought of as collisionless. If individual encounters are elastic, then the system will conserve the sum of kinetic and potential energy, and the clustering will be dissipationless.

2.2 SPH

In SPH, densities and gas forces at particle locations are calculated as a summation of pairwise contributions. No grid is involved in the dynamics, so the resolution is essentially controlled by the mean interparticle spacing. The pairwise contributions fall off rapidly with separation beyond a smoothing scale h as detailed below. Mechanically, this means the gas interactions are readily inserted into the routine handling the calculation of $g_i^{SR}(r_c)$ as long as $h \lesssim r_c$. This makes the coupling of SPH with P3M quite natural.

The technique employed to determine local densities and pressure gradients is known as kernel estimation. The process is equivalent to convolving a field $f(\mathbf{x})$ with a smoothing, or filter, function $W(\mathbf{r} - \mathbf{x}, h)$ to produce a smoothed estimate of the field $f_s(\mathbf{r})$

$$f_s(\mathbf{r}) = \int d^3x \, f(\mathbf{x}) \, W(\mathbf{r} - \mathbf{x}, h). \tag{5}$$

The kernel $W(u, h)$, where $u = |\mathbf{r} - \mathbf{x}|$, is assumed to be spherically symmetric, normalized to $\int d^3u W(u, h) = 1$, and is compact on the scale h,

$$4\pi \int_0^h du u^2 W(u, h) \simeq 1.$$

A fiducial choice is a Gaussian

$$W(u, h) = \frac{1}{\pi^{3/2} h^3} \exp\left(-u^2/h^2\right). \tag{6}$$

If we take $f(\mathbf{x})$ to be the density field arising from the discrete distribution of gas particles

$$f(\mathbf{x}) \rightarrow \varrho(\mathbf{x}) = m_g \sum_j \delta(x - x_j), \tag{7}$$

then the smoothed density estimate of the discrete field is simply

$$\varrho_s(\mathbf{r}) = m_g \sum_j W(|\mathbf{r}-\mathbf{r}_j|, h). \tag{8}$$

In particular, the estimate of the density for particle i is

$$\varrho_i = m_g \sum_j W(r_{ij}, h). \tag{9}$$

The estimate, equation (9), assumes a uniform smoothing scale h over all space. This is unnecessary and will severely impair the ability to resolve the multiple levels of substructure present in typical cosmological simulations. It is much better to employ a smoothing which varies with both position and time in order to dynamically adapt the resolution to local conditions. Each particle is thus labelled with a smoothing scale h_i, and the density estimate for particle i is equation (9) with h_i replacing h. Intuitively, one would expect h_i to scale with the local interparticle separation, so that the smoothing should be dynamically adapted with time according to the relation

$$\frac{\delta h_i}{h_i} = -\frac{1}{3}\frac{\delta\varrho_i}{\varrho_i}, \tag{10}$$

where $\delta\varrho_i$ is the change in density at the location of particle i over one timestep. This insures a roughly constant number of neighbours within a sphere of radius h_i around any particle at all times. Static tests presented in the next section will demonstrate the improved dynamic range of variable smoothing. More details on variable h are given in the Appendix.

Given the local density ϱ_i and the thermal energy ϵ_i, the equation of state $P_i = (\gamma-1)\epsilon_i\varrho_i$ specifies the pressure at the location of particle i. A smoothed estimate of a gradient of some function f is the same as that function convolved with the gradient of the smoothing kernel

$$(\nabla f(\mathbf{r}))_s = \int d^3x\, \nabla f(\mathbf{x})\, W(\mathbf{r}-\mathbf{x}, h) = \int d^3x\, f(\mathbf{x})\nabla W(\mathbf{r}-\mathbf{x}, h). \tag{11}$$

To estimate the pressure gradient term in the equation of motion (2b), it is better to rewrite it as

$$-\left(\frac{\nabla P}{\varrho}\right) = -\nabla\left(\frac{P}{\varrho}\right) - \left(\frac{P}{\varrho^2}\right)\nabla\varrho. \tag{12}$$

This gives the gas force acting on particle i as a sum of antisymmetric interactions with its neighbours j

$$\mathbf{F}_i^{gas} \equiv -\left(\frac{\nabla P}{\varrho}\right)_i = -m_g \sum_j \left(\frac{P_i}{\varrho_i^2} + \frac{P_j}{\varrho_j^2}\right)\nabla W(r_{ij}, h_{ij}), \tag{13}$$

where $h_{ij} = \frac{1}{2}(h_i + h_j)$ is used to preserve the symmetry. The form of equation (13) guarantees conservation of linear and angular momentum when a spherically symmetric kernel is used. The adiabatic change in internal energy is found in similar fashion to be

$$\frac{d\epsilon_i}{dt} = m\left(\frac{P_i}{\varrho_i^2}\right)\sum_j \nabla W(r_{ij}, h_{ij})\cdot\mathbf{v}_{ij}. \tag{14}$$

For high mach number collisions, thermal pressure is not sufficient to prevent free streaming of the gas particles. For real gases, molecular viscosity is effective in stopping penetration within roughly a molecular mean free path. To achieve the same result in the hydrodynamic simulation

(on a length scale comparable to the mean free paths of the model particles) an artificial viscosity is introduced. The viscosity effectively increases the pressure in regions of strongly converging flow from ϱc^2 to $\sim \varrho v^2$. Various forms of SPH viscosity have been considered in the literature (Monaghan & Gingold 1983; Loewenstein & Mathews 1986; Lattanzio *et al.* 1986). Two forms are employed in this paper. For the self-gravitating collapse presented in the next section, the form adopted follows that used by Lattanzio *et al.* (1985, 1986) to control interpenetration of colliding molecular clouds. This viscosity multiplies the pressure experienced by an individual approaching pair with a term of the form $[1 + \alpha_1(v/c)(h/r) + \alpha_2(v/c)^2(h/r)^2]$. More precisely, the summands on the right hand sides of equations (13) and (14) now include the term $(1 + \alpha_1 q_{ij} + \alpha_2 q_{ij}^2)$, where

$$q_{ij} = \begin{cases} [|\mathbf{v} \cdot \mathbf{r}|_{ij}/(ch)_{ij}] \, [(r/h)_{ij}^2 + \eta^2]^{-1}, & (\mathbf{v} \cdot \mathbf{r})_{ij} < 0, \\ 0 & , & (\mathbf{v} \cdot \mathbf{r})_{ij} > 0, \end{cases} \tag{15}$$

and $(ch)_{ij}$ is the product of the mean sound speed and smoothing lengths for particles i and j. The free parameters α_1, α_2 and η^2 are set by comparison with shock-tube problems, typically $\alpha_1 \sim 1$, $\alpha_2 \sim 2$ and $\eta^2 \sim 0.01$ (Lattanzio *et al.* 1986).

   The second viscosity employed in the cosmological example of the next section is similar in form to the above, in that $P \rightarrow P[1 + \beta_1(v/c) + \beta_2(v/c)^2]$. However, the magnitude of the artificial pressure is not solely calculated on a per interaction basis. Instead, an individual artificial pressure Q_i is defined for each particle by

$$Q_i = \beta_1 c_i q_i + \beta_2 q_i^2/\varrho_i, \tag{16}$$

where

$$q_i = \sum_j \delta v_{ij} \, W_{ij} \tag{17}$$

$$\delta v_{ij} = \begin{cases} (|v_x| + |v_y| + |v_z|)_{ij} & , & (\mathbf{v} \cdot \mathbf{r})_{ij} < 0, \\ 0 & , & (\mathbf{v} \cdot \mathbf{r})_{ij} > 0. \end{cases} \tag{18}$$

Note that q_i has dimension of ϱv. During the force calculation, approaching pairs have $P \rightarrow P + Q$ in equations (13) and (14). This form is similar to that studied in a standing shock wave by Loewenstein & Mathews (1986). Values of $\beta_1 \sim 0.5$, $\beta_2 \sim 2$ produced good results in shock tube experiments. The results are insensitive to variation of these parameters by factors of ~ 2.

2.3 COMBINING THE TWO METHODS

The fixed timestep in P3M is governed by the gravitation softening

$$\delta t < c_1 \varepsilon^{3/2}, \tag{19}$$

where c_1 is a constant of order unity. For the gas, it is necessary to satisfy the Courant condition

$$\delta t < c_2 \min\left\{\frac{h}{c}\right\}_i, \tag{20}$$

where c_2 is another constant of order unity. Most hydrodynamic codes use a variable timestep, appropriately adjusted to satisfy equation (20). If we take the simplest route and retain the fixed timestep nature of P3M, then we can turn the Courant condition around to give a lower bound on the resolution length

$$h_i > \frac{1}{c_2} (c_i \delta t). \tag{21}$$

The local smoothing h_i is now governed dynamically by the local density variations, equation (10), but subject to the above constraint calculated for each particle at each step.

A schematic of the actions taken during the advance of one timestep is outlined in Fig. 1. The gas particles' positions, velocities, smoothing lengths, and specific thermal energies are specified as input. First, new densities ϱ^n are calculated using the old smoothings h^{n-1}. The change in density is then used to update the smoothing. Since the thermal energy is not time-centred, a linear extrapolation is done to determine ϵ^n for the quantity $(P/\varrho^2)^n$ needed in the force calculation loop. Next, the long-range component of the gravity is added to all species. The short-range pair correction to the gravity is then done for all species' interactions. For gas–gas pairs, the SPH forces are also added to the momenta, and their internal energies updated. Finally, the positions are advanced using the updated velocities $v^{n+1/2}$ and the process is ready to repeat at step $n+1$.
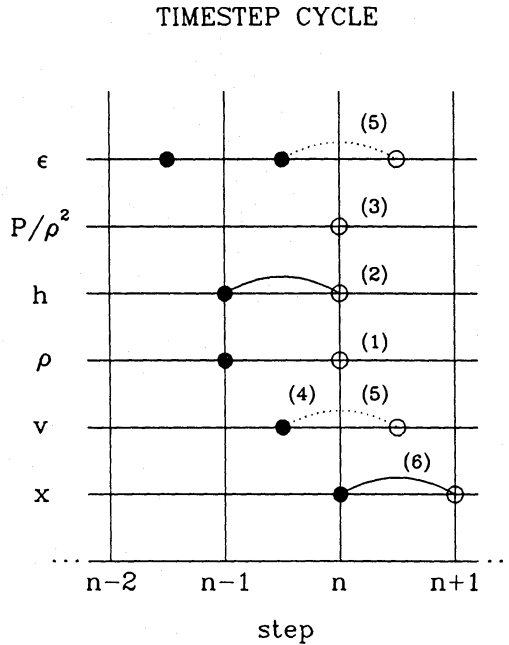
TIMESTEP CYCLE

Figure 1. Outline of actions taken to advance one timestep. Information brought into step n is shown as filled circles, open circles are quantities calculated at that step. (1) With x^n and h^{n-1}, get new densities ϱ^n. (2) Update smoothing using $h^n = h^{n-1}[1 - 1/3(\varrho^n - \varrho^{n-1})/\varrho^{n-1}]$. (3) Predict $(P/\varrho^2)^n$ from $\epsilon^{n-1/2}$ and $\epsilon^{n-3/2}$. (4) Add mesh gravity to momenta. (5) Add short-range gravity and gas forces, update internal energies. (6) Move positions to next timestep.

3 Tests

As outlined in the Introduction, an important ingredient for application of the code to cosmological problems is the ability to follow the shock-heating of initially cold gas through gravitational collapse. To test this process, cold collapses of spherically symmetric systems modelled with SPH are compared with solutions obtained using a 1D Lagrangian finite difference code. This is done both for a self-gravitating isolated sphere and for a spherical perturbation with 90 per cent dark matter in a flat cosmology.

Before considering these more complex dynamical tests, it is useful to demonstrate the capability of the kernel estimation method to measure local densities and density gradients. To this end, static tests are performed on realizations of known density distributions. Another useful check on the code is to reproduce an analytic solution, where analytic here includes problems

reduced to ordinary differential equations solvable by standard techniques. The problem examined below is the self-similar adiabatic expansion of an initially isothermal gas cloud.

3.1 STATIC TESTS

As a first test, it is reasonable to ask whether the expression for the local density, equation (9), can accurately measure the density of, say, a unit lattice. However, we know that our simulated systems will be of finite size. It would be more informative, then, to cut a sphere out of the lattice and ask how the measured density is affected by the system's finite size. The results are displayed in Fig. 2. Unit lattice spacing is assumed, and the density at the origin is calculated by equation (9) over a range of h using only those particles within a distance R of the origin. Values of R range from 1 to 10 in unit increments. The Gaussian kernel, equation (6), is used. For very large R, a wide range of values for h reproduce the true density accurately. As R decreases, the density is seen to be substantially underestimated when $h \gtrsim R/2$. On the other hand, if h is chosen too small, the contribution from the particle at the origin dominates and the density estimate diverges as h^{-3}.

In many calculations, initial conditions are set up using a perturbed grid. Fig. (2a) then suggests using initial values of h approximately 1.2–1.4 times the local grid spacing in order to have the capacity to resolve clumps down to a few tens of particles (corresponding to $R \approx 2-3$). After the initial specification, the particle smoothings are updated dynamically, subject also to the Courant limit. As a final precaution against h getting too small, h is not allowed to decrease if $h^3 \varrho \lesssim 3$ (straight line in Fig. 2b). This puts a limit of $h \gtrsim \sqrt{2}$ times the local interparticle separation, implying there are $\gtrsim 18$ neighbours contributing significantly to the interactions of each particle.

Results of another static test using a radially decreasing density profile are shown in Fig. 3.
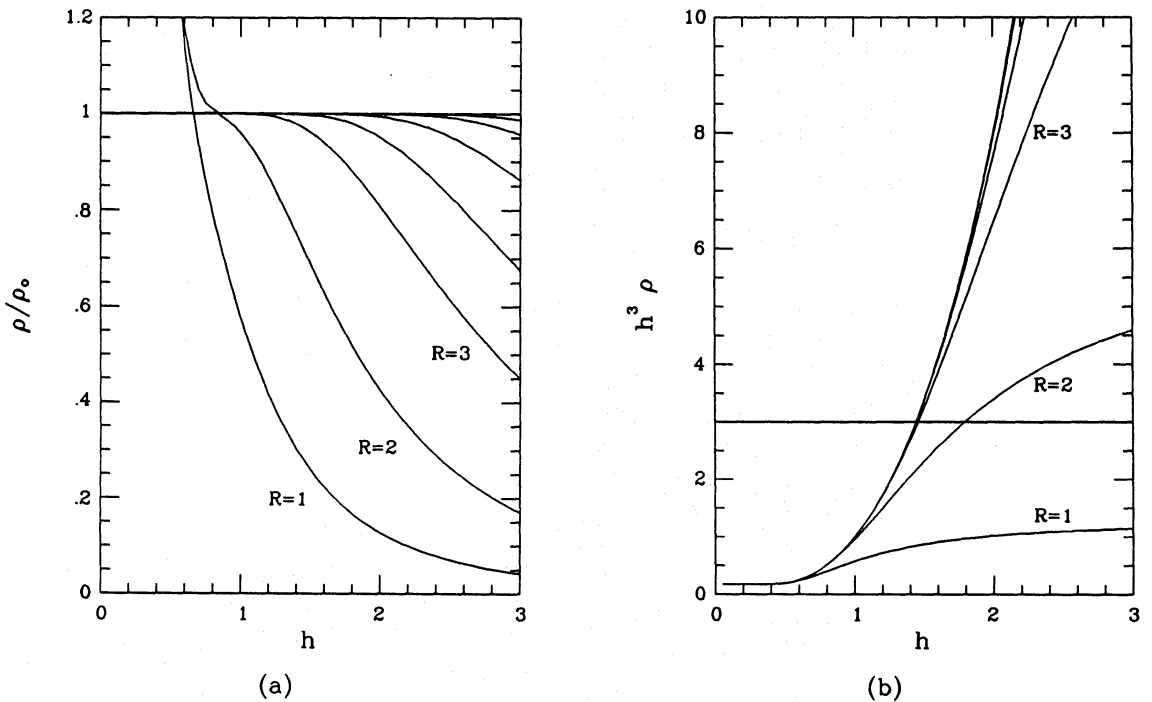

Figure 2. (a) Density estimates at the centre of a sphere of radius R cut from a unit cubic lattice, as a function of the smoothing radius h. Choosing a value of h only slightly larger than the grid spacing allows definition of systems as small as $R \sim 2-3$. (b) The quantity $4\pi h^3$ gives roughly the number of particles contributing significantly to the hydrodynamics of each particle. During the dynamic control of the resolution, h_i is not allowed to decrease if $h_i^3 \varrho_i < 3$. This prevents any possible runaway in the small h regime shown in (a).
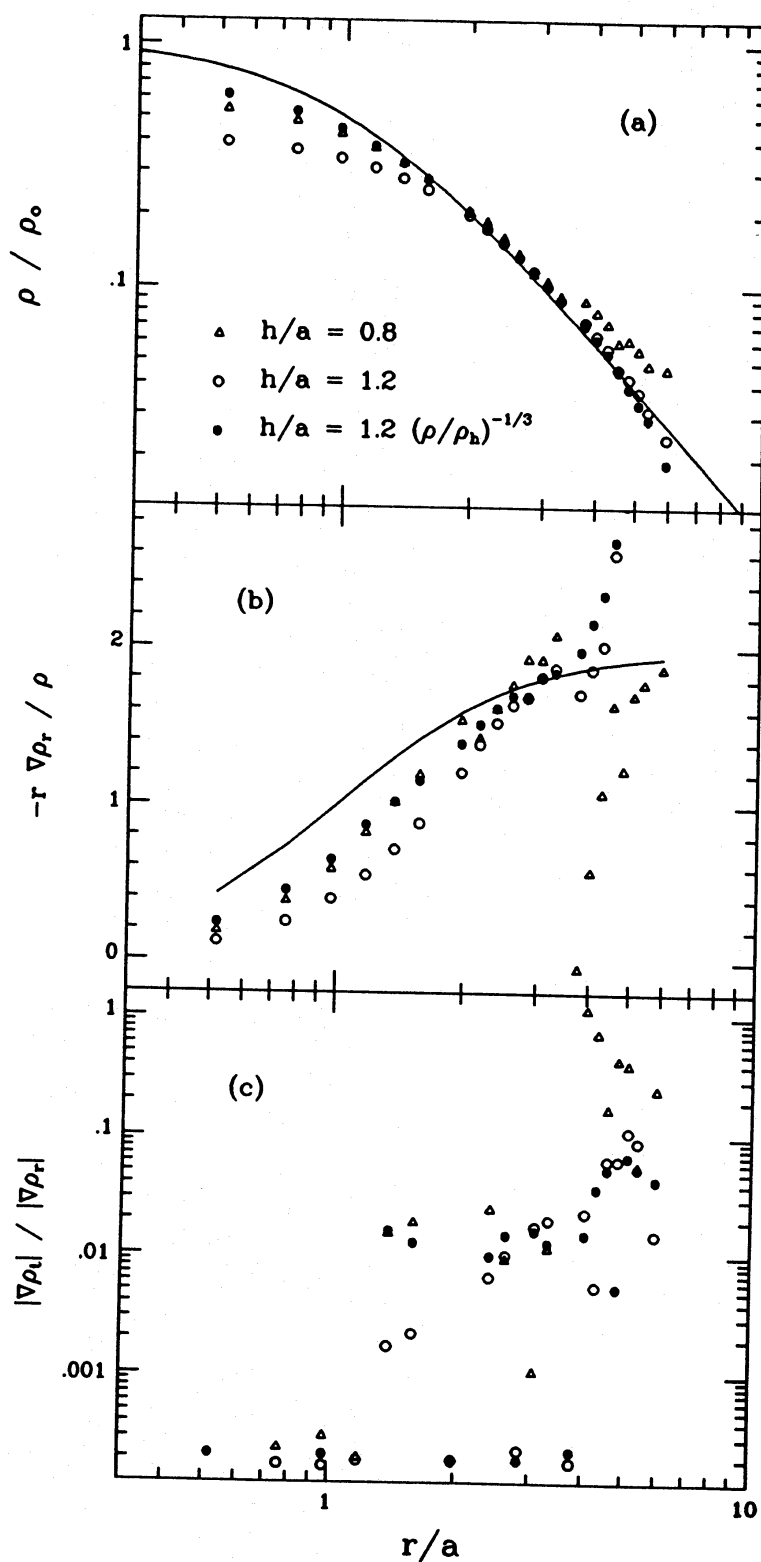
Figure 3. Static test on a realization of the density profile $\varrho(r)=\varrho_0[1+(r/a)^2]^{-1}$: (a) density estimates for variable smoothing (solid circles) and uniform smoothing (open symbols); (b) dimensionless measure of the radial gradient; (c) anisotropy measured by the magnitude ratio of tangential to radial components of the density gradient. Results expected from the assumed density profile are shown as solid lines in (a) and (b).

Particles initially on a grid are perturbed radially so that the resultant mass distribution follows that of an isothermal sphere, $\varrho(r)=\varrho_0[1+(r/a)^2]^{-1}$. The sphere is truncated at six core radii, leaving 485 particles within the finite sphere. The local density and density gradient (radial and tangential components) were estimated with a Gaussian kernel. This was done using spatially constant h and an h varying with the inverse cube root of the given density profile. Fig. 3(a) shows that the variable h estimates more accurately reproduce the exhibited density range than do the constant h estimates. Choosing a small constant value for h (open triangles) can reasonably resolve the core density, but this leads to overestimates in the outer parts where $h \lesssim$ one-half the local interparticle spacing. A larger constant value (open circles) succeeds in the outer regions but underestimates the central density by a factor of 2. With variable h (filled circles), the local smoothing scale ranges from $h \approx 0.6$ in the centre to $h \approx 1.8$ at the outer edge. Neglecting the particles just on the outer boundary (for which the density should be underestimated because of the surrounding void), the maximum error in the estimated density is about 25 per cent in the centre. The accuracy for the bulk of the mass is much better, typically a few per cent.

Estimates of the radial density gradient are shown in Fig. 3(b), using the dimensionless combination $-r(\nabla\varrho)_r/\varrho$. The gradient is more poorly reproduced than the density. With variable h, the magnitude is underestimated by a constant amount below two core radii, while the sharp boundary causes an overestimate for radii within h of the outer edge. Using a smaller normalization for h can improve the agreement at small r, but only at the cost of increasing the sensitivity to the grid anisotropy at larger radii. A measure of the anisotropy, the ratio of the tangential to radial components of the gradient, is shown in Fig. 3(c). In the dynamic tests below, we use such 'stretched grid' configurations as initial conditions approximating spherically symmetric mass distributions. If a fair comparison is to be made between the code and other solutions based on spherical symmetry, the anisotropy in the estimated gradients should be small. From Fig. 3(c), the anisotropy is less than 2 per cent at radii interior to $\sim h$ from the boundary. For variable h, the largest anisotropy is ~ 8 per cent at radii close to the edge. As with the density estimate, the same qualitative statements can be made regarding constant h for the gradient and anisotropies. No single value can be found to yield as good agreement throughout the full range of the system shown.

3.2 SELF-SIMILAR ADIABATIC EXPANSION

A stringent test of a numerical method is a test for self-similarity. Often, it is not possible to construct a numerical system which will behave in self-similar fashion, as artificial scales involved in the calculation (from boundary conditions, finite resolution scales, etc.) may ruin the scaling properties of the original differential equations. Even so, there is typically a window within which the numerical system may behave in self-similar fashion.

The test presented here involves the adiabatic expansion of an unbounded, initially isothermal, $\gamma=5/3$ sphere. The initial system has a density profile $\varrho(r)=cr^{-2}$, a constant temperature T_0, and a radial velocity field specified by $v(r)=q_0 v_{\rm ff}(r)$ where $v_{\rm ff}(r)$ is the free-fall velocity at radius r which in this case is constant. A family of solutions is found dependent on the self-similar variable

$$Y=(cG)^{1/2}r^{-1}t. \tag{21}$$

The method of solution is similar to that of Yahil (1983), who extended the earlier work of Goldreich & Weber (1980). The self-similar density, thermal energy, and velocity are defined by

$$\varrho(r,\,t)=cr^{-2}\,D(Y), \tag{22a}$$

$$\epsilon(r,\,t)=\epsilon_0 E(Y), \tag{22b}$$

$$v(r,\,t)=q_0(8\pi cG)^{1/2}V(Y). \tag{22c}$$

Re-writing the continuity equation and Euler's equation in terms of the self-similar variables gives two coupled ordinary differential equations which can be integrated in standard fashion from the initial state at $Y=0$. A family of solutions arises from different values for the initial temperature and velocity field.

We examine an initially expanding sphere with $q_0=0.5$ and an initial temperature chosen such that the magnitude of the pressure gradient is 1.5 times the gravitational force at all radii. A finite sphere of radius R containing 485 particles is used in the calculation. The r^{-2} initial density profile is achieved by radial stretching of a uniform grid, $r_i^{old} \rightarrow r_i^{new} = (r_i^{old}/R)^3 R$. Variable smoothing is employed, the initial values of h_i are scaled with the local interparticle separation. The system expands by a factor of ~ 2 within roughly a time t_*, where $t_* = (3\pi/32G\bar{\varrho})^{1/2}$ is the free-fall time at the outer boundary.

Fig. 4(a) shows the evolution of the density, temperature, and velocity profiles of the sphere in physical units at times $t/t_* = 0.0, 0.2, 0.5$ and 0.8. The corresponding evolution in terms of the self-similar variables is shown in Fig. 4(b). As the system expands, the pressure gradient drops as $r^{-7/3}$ while the gravitational acceleration falls as r^{-2}. The system thus slides delicately from being pressure driven to gravity dominated. Boundary effects are evident in the evolution shown in Fig. 4(b). The lack of confining pressure allows the outer boundary to expand faster than the self-similar behaviour, resulting in lower densities and temperatures for small Y. As the system evolves, these boundary effects propagate through the model (the second crossing time is of order t_* in this calculation), so that at times $t \gtrsim t_*$, the entire system will not be self-similar. For small values of r (large Y), the finite resolution of the calculation causes departures from the self-similar behaviour. In between these regimes, there is a narrow (factor of ~ 2) range in which the
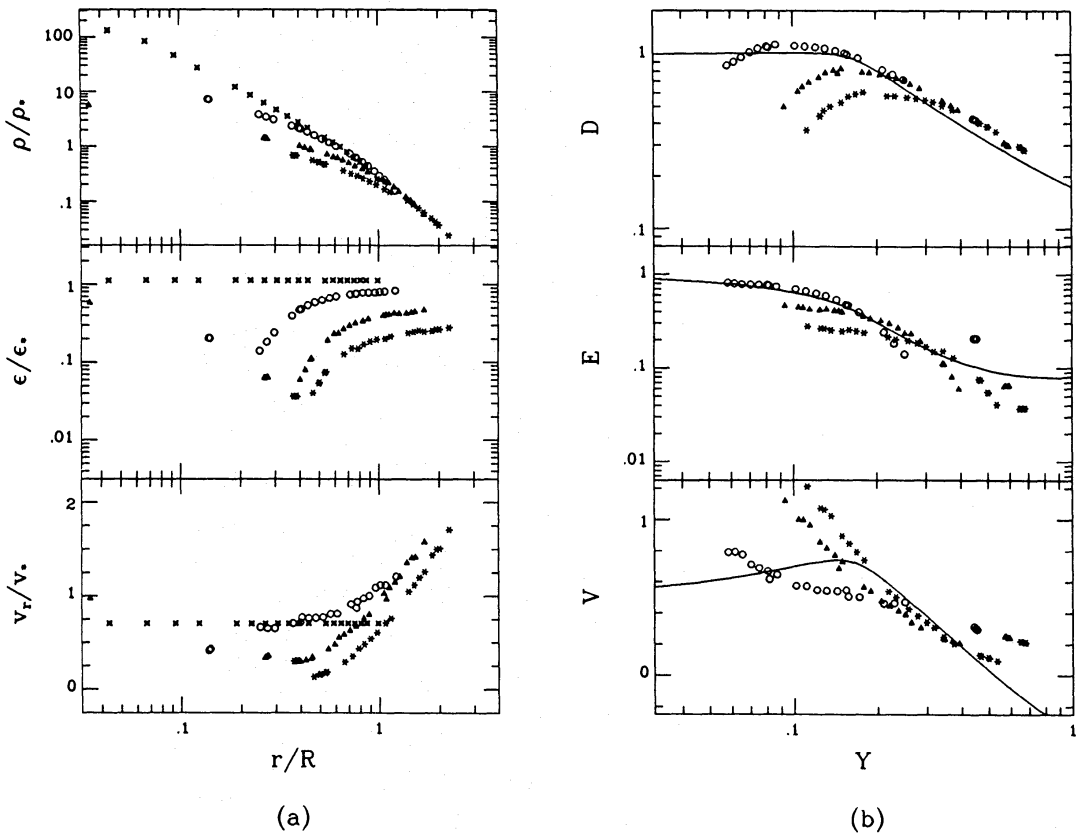

Figure 4. Evolution of the density, temperature, and radial velocity of an expanding gas sphere. (a) Development in physical units; (b) evolution in terms of the self-similar variables defined in Section 3. Symbols represent different times: crosses, $t=0$; open circles, $t=0.2t_*$; triangles, $t=0.5t_*$; asterisks, $t=0.8t_*$.

self-similar solution is reproduced to an accuracy of ~10–20 per cent. Considering that the central pressure drops by over three orders of magnitude from $t=0$ to $t=0.8t_*$, and considering the fact that the finite system is only a few h wide, this level of agreement is quite acceptable.

3.3 SELF-GRAVITATING COLLAPSE OF A COLD GAS SPHERE

In this test, a comparison is made between P3MSPH and an accurate 1D Lagrangian finite difference code (Thomas 1987) applied to a spherically symmetric collapse problem. The initial state consists of a static gas sphere of mass M_t and radius R, with a shallow density profile, $\varrho(r) \propto r^{-1}$. The initial temperature is much smaller than the virial temperature. The particle distribution is set up using the same procedure as above, again with 485 particles. There are 250 cells, initially spaced at equal intervals of r, in the 1D calculation, providing a detailed look at the shock-heating process.

The evolution of the system is shown in Fig. 5, the P3MSPH solutions are the dotted lines, the 1D results are shown by solid lines. Scales used are: density, $\varrho_* = 3M_t/4\pi R^3$; energy, $\epsilon_* = GM_t/R$; pressure, $P_* = \varrho_* \epsilon_*$; and velocity, $v_* = (GM_t/R)^{1/2}$. Time is again given in terms of the free-fall time at the outer radius, $t_* = (\pi^2/8)^{1/2} R^{3/2} M_t^{-1/2}$. Initially far from equilibrium, the system collapses,
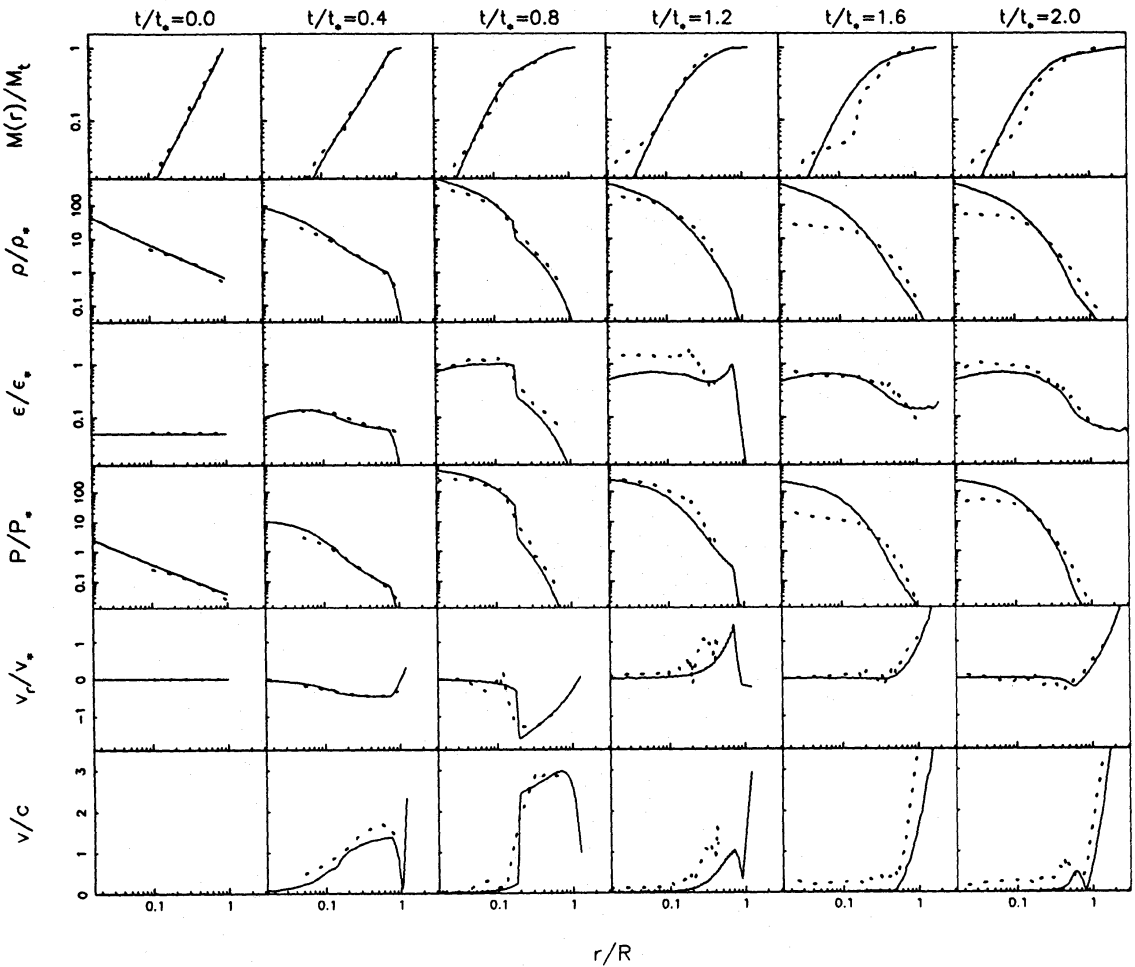

Figure 5. Results of self-gravitating cold collapse problem. Time evolution of the radial profiles of, from top to bottom, enclosed gas mass, density, thermal energy, pressure, radial velocity, and Mach number. Each vertical panel gives profiles at the time specified at the top of the frame. Solid lines are results of a 1D Lagrangian finite difference code, dashed lines are from P3MSPH.

converting most of its kinetic energy into heat between $t\sim0.8t_*$ and $t\sim1.2t_*$. A slight expansion follows as a small outer mantle is blown off, and by $t\sim2t_*$, the system is very close to an equilibrium state. The total energy of the system is conserved to ~1 per cent, with momentum and angular momentum conservation better than 10^{-3}.

In general there is good agreement in the temporal evolution of the system profiles. At $t=0.44t_*$, the central regions are being adiabatically compressed and a weak shock is beginning to develop. By $t=0.8t_*$, the shock has propagated through roughly half the total mass. There is good agreement between the two codes on the position of the shock front and the temperature profile behind the shock. The factor of 4 jump in density evident in the 1D calculation is smeared over a distance $\sim h$ in P3MSPH and so is washed into the radially decreasing density profile. The P3MSPH system is slightly delayed coming out of the point of maximum collapse, probably caused by underestimate of the pressure gradients at $t\approx t_*$ when most of the mass in the system is crunched to barely $2h$ in radius. Thus the 3D system at $t/t_*=1.2$ is smaller and hotter than its 1D counterpart. By $t/t_*=1.6$, the system has fully rebounded and at $t/t_*=2.0$, it has essentially reached an equilibrium configuration consisting of a hot, nearly isothermal core and a rarified, adiabatically cooling halo. In the central post-shock region, the smallest value of h consistent with the Courant limit is $h\approx0.1R$. This resolution limit is apparent in the density profile, where the P3MSPH density is an underestimate for $r\lesssim0.1R$.
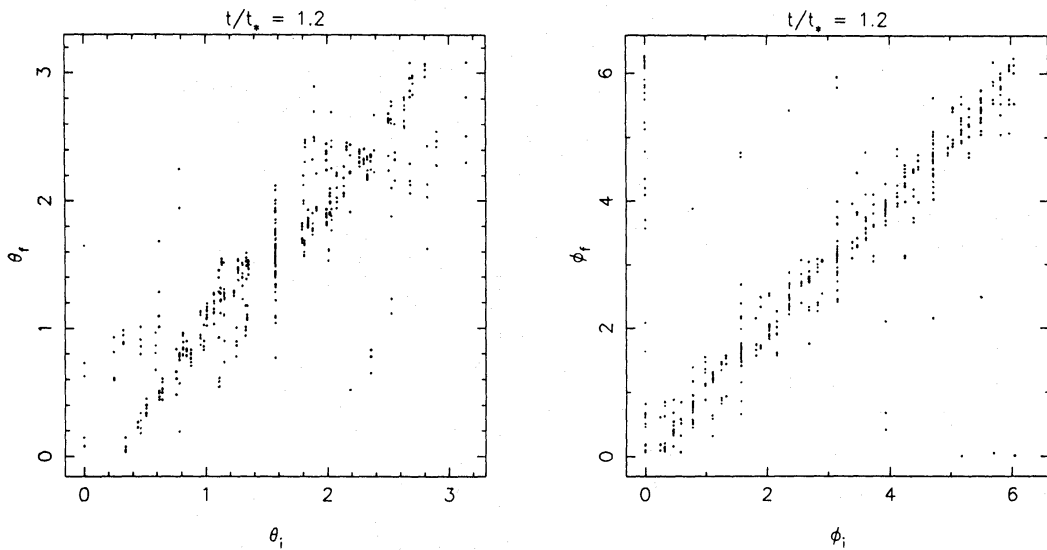

Figure 6. Test of free streaming for the system shown in Fig. 5. Final angular coordinates are well correlated with their initial values, indicating little gas interpenetration.

A test of the artificial viscosity's ability to prevent free-streaming of the gas is shown in Fig. 6. Here, the particles' final angular coordinates (θ, ϕ) are plotted against their initial values at a time just after rebound. Free streaming would produce a characteristic X-shape in the θ_f versus θ_i diagram and side lobes displaced $\pm\pi$ off the diagonal in the ϕ_f versus ϕ_i diagram. There is no evidence for significant streaming in Fig. 6. In fact, the rms total angular displacement of the particles is less than $20°$, showing that the 3D particle trajectories are very close to radial.

A check on the effectiveness of the viscosity to damp random particle motions is exhibited in Fig. 7. A projection of the particle distribution in a cube of side $L\approx0.6R$ is shown at $t/t_*=1.2$. Velocities projected on to the plane originate from each particle's location. Characteristic scales to the right of the plot show the central sound speed c_s, minimum smoothing h_{min}, and the gravitational softening parameter ε. The radial blowoff of an outer mantle of material is clear
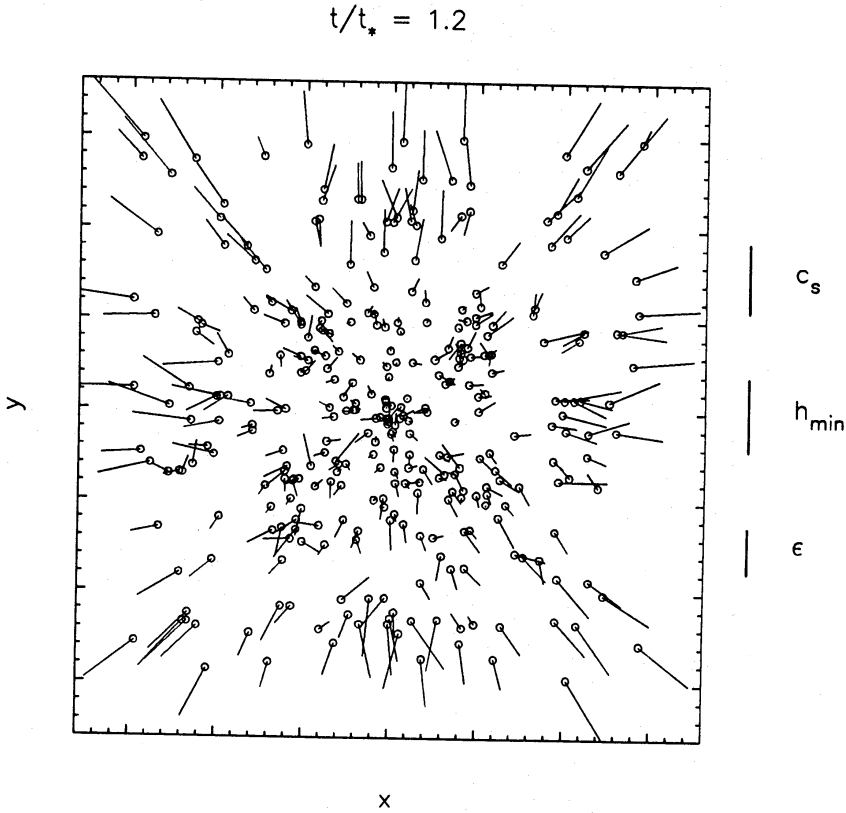
$$t/t_* = 1.2$$

Figure 7. The particle distribution at $t/t_* = 1.2$ in the self-gravitating collapse problem. Projected particle positions and velocity vectors are shown in a central region of width $L \simeq 0.6\,R$. The magnitudes of the post-shock sound speed c_s, lower bound on smoothing h_{min}, and gravitational softening ε are shown for comparison. The central velocity dispersion is small compared to the sound speed.

from the picture. The magnitude of the central velocity dispersion is roughly 10–20 per cent the sound speed, indicating a small ratio of kinetic to thermal pressure $\sigma^2/c_s^2 \lesssim 5$ per cent.

It is encouraging that the 3D P3MSPH results agree so well with the high resolution 1D calculation. The agreement is particularly impressive if one takes $\frac{1}{2}(485)^{1/3} \simeq 4$ as a naive measure of the number of radial 'cells' in the 3D calculation.

3.4 SPHERICALLY SYMMETRIC PROTO-CLUSTER COLLAPSE

As a final test and one most relevant to the intended use of the code, the turnaround and collapse of a spherical perturbation in a flat ($\Omega = 1.0$) cosmology consisting of 90 per cent dark matter and 10 per cent gas is studied. Again, the P3MSPH results are compared to those of the 1D spherically symmetric code, modified to include collisionless shells of dark matter. The dark shells experience no pressure and are allowed to stream freely through the origin. The resultant collapse produces a nearly pure power-law density profile for the dark matter. This is inconsistent with realistic 3D collapse models (van Albada 1982; McGlynn 1984), where violent relaxation and merging of inhomogeneous substructure typically produce core–halo structures. Inclusion of artificial angular momentum barriers to mimic the isotropization that occurs during violent relaxation can succeed in producing a core–halo structure in the 1D simulation. However, since the 3D models also contain no angular momentum initially, the particles will closely follow radial trajectories, hence no modification of the free-streaming treatment of dark shells in the 1D code is necessary if a fair comparison of the two results is to be made.

The initial perturbation consists of a single radial cosine wave. The treatment is identical to that Peebles (1982) used to set up a proto-void, the sign is simply reversed to give a proto-cluster. Given a uniform sphere of radius x_t, one perturbs comoving radii by

$$\mathbf{x}_0 \rightarrow \mathbf{x}_1 = \mathbf{x}_0[1 - \delta(x_0)/3] \qquad (23)$$

and sets peculiar velocities according to growing mode linear theory

$$\mathbf{v} = -\frac{2}{3} H \mathbf{x}_0 \delta(x_0), \qquad (24)$$

where

$$\delta(x) = 0.5 \, \delta_0 [1 + \cos(\pi x / x_t)]. \qquad (25)$$

The initial perturbation has $\delta_0 = 1$, and is scaled to a size appropriate to rich clusters of galaxies. There are 1791 gas particles and an equal number of collisionless particles within x_t. The model is begun at a redshift $z = 4$ and has a total mass $M_t = 3 \times 10^{15} M_\odot$ giving it a comoving radius of $x_t \simeq 22$ Mpc for $H_0 = 50$ km s^{-1} Mpc^{-1}. The initial gas temperature is $T = 10^5$ K. Note the density perturbation is zero at $x = x_t$, so the outer edge is freely expanding.

The detailed evolutions of the system are shown in Fig. 8 using physical units. The shock front is
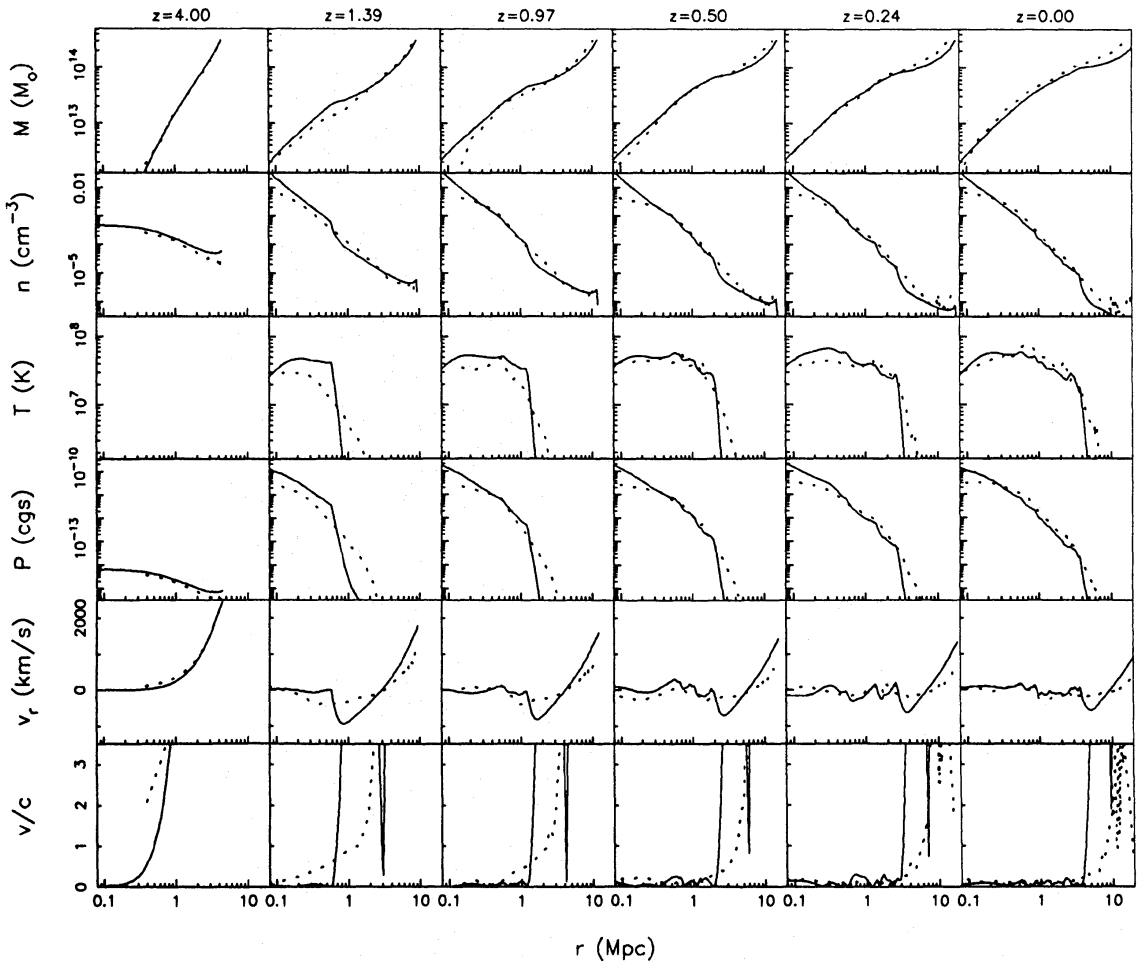

Figure 8. Evolution of the gas in the two-component rich cluster collapse. Format is identical to Fig. 5. Redshift of each vertical frame is given at the top of the panel.

somewhat ill-defined in P3MSPH until a redshift $z \simeq 1$, when more than ~ 100 particles have passed through the shock, after which the front radius and post-shock temperature are well defined. Good agreement is found in this regime with the 1D evolution. At the final epoch, the density profiles agree over three orders of magnitude to an rms accuracy of better than 15 per cent. Below the resolution limit of ~ 200 kpc, the P3MSPH density falls below the 1D result. The temperature profiles over one and one-half magnitudes in radius agree to within 25 per cent (rms). The presence of radial sound waves in the post-shock regimes of both calculations means that exact agreement cannot be expected. In both calculations, typical random velocities of the gas behind the shock are small, $v/c \approx 0.1$–0.2.

A revealing plot of the viscosity's success in preventing interpenetration of the gas in this two-component model is shown in Fig. 9. The top two frames show the gas particle distribution at a redshift $z=0.5$, along with projected velocity vectors, the bottom two panels show the dark particles. The left panels of both top and bottom contain only those particles which *began* the simulation on that side [i.e. had $x(z=4)<0.5$]. The right panels similarly show those particles which originated on that side [$x(z=4)>0.5$]. Free-streaming is evident for the collisionless dark-matter particles, while the gas shows little evidence for interpenetration. The other noticeable
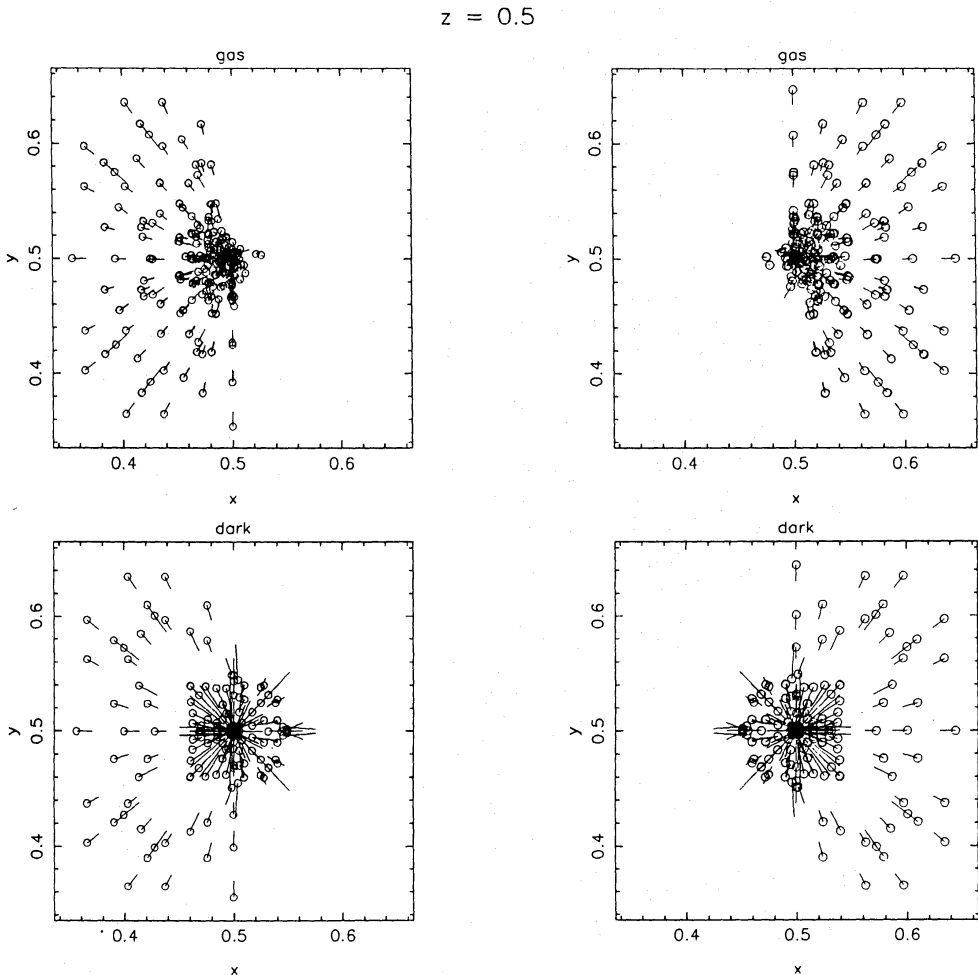

Figure 9. Free streaming demonstration in the two-component model. The left panels show projected positions and velocities at $z=0.5$ of only those particles which *began* the simulation on that side ($x<0.5$), and vice-versa for the right-hand panels. The upper panels show the gas, the lower are the dark particles. The collisionless dark particles readily free-stream, while the gas viscosity is evidently effective at preventing interpenetration.

difference in the two particle distributions is the degree of spherical symmetry. The dark particles, being collisionless, retain the memory of their original grid structure, as evidence by the square-edged configuration seen in the bottom panels of Fig. 9. In contrast, the gas particle distribution appears fairly isotropic in projection, the sharp-edged features of the initial conditions having been smoothed over by the pressure gradients.

Finally, a detailed comparison of the properties of the cluster core is given in Fig. 10. The core at a redshift z is defined by the radius at which the mean interior density equals a constant value times the background density at that redshift. Here, the mean overdensity is chosen to be 170 times the background, the value expected in the virialized regime from simple top-hat arguments (Kaiser 1986). The core radius, interior gas mass, mean temperature and total X-ray luminosity
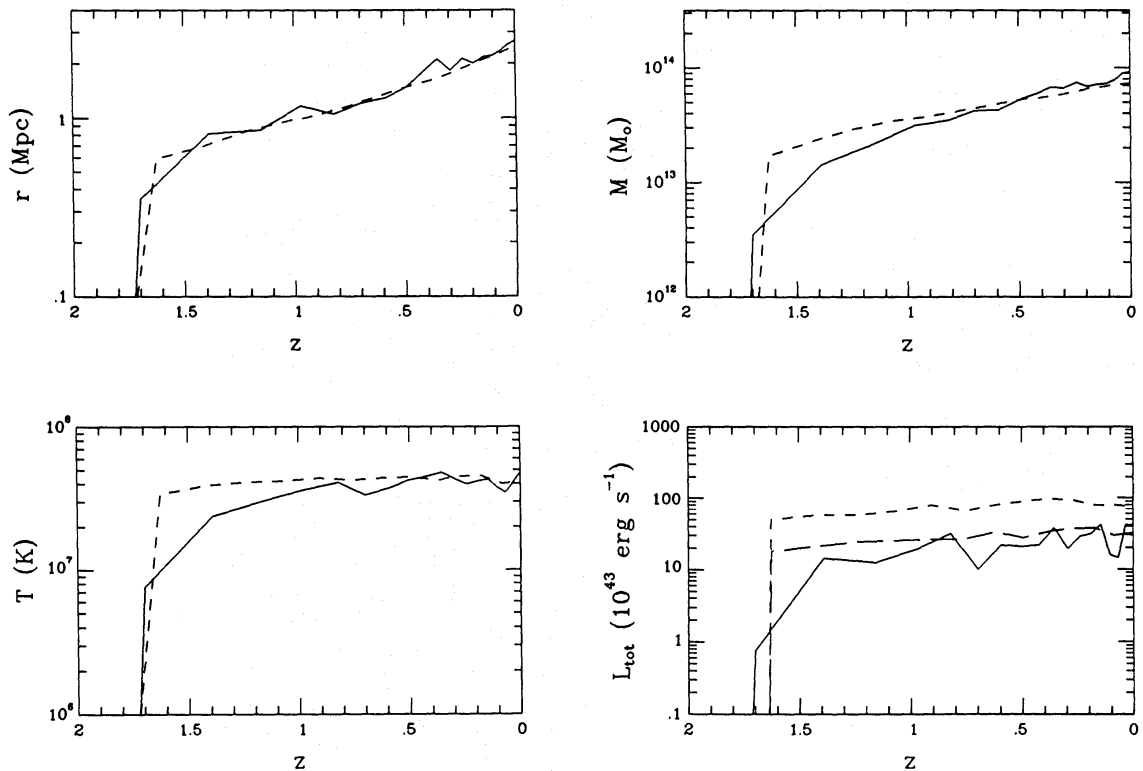

Figure 10. Redshift evolution of the core properties of the rich cluster. The core radius r, enclosed gas mass M, mean temperature T and total X-ray luminosity L_{tot} are shown. Solid lines are the P3MSPH results, short dashed lines are from the 1D Lagrangian. The long dashed line in the L_{tot} plot is the 1D result with the inner 200 kpc emission removed.

are shown as a function of redshift, with the P3MSPH results given by solid lines, the 1D as dashed lines. The agreement is very good for all quantities save the luminosity, which is low in P3MSPH by a factor of ~3. The discrepancy results from the much higher resolution of the 1D calculation – since $L_x \propto \varrho^2 T^{0.5}$, a significant contribution to the luminosity can be made by a relatively small amount of mass at high density. When the resolution of the 1D code is reduced to that of the 3D code (~200 kpc), the agreement is much improved, as shown by the long dashed line in Fig. 10.

The resolution limits of the 3D P3MSPH should not pose a serious problem for determining X-ray luminosities in realistic 3D collapses, where core–halo density structures are expected. As long as the resolution is sufficient to define the core density value, the luminosity will be accurately estimated. The topic of resolution is addressed in more detail in the following section.

4 Resolution estimates

To give an idea of the type of calculation accessible to experiment on present microcomputers (e.g. a μVAX), some characteristic parameters for simulations on two scales of interest, galaxies and rich clusters, are presented here. The data are summarized in Table 1. A background cosmology with $\Omega=1$, 10 per cent gas and $H_0=50\,\mathrm{km\,s^{-1}\,Mpc^{-1}}$ is assumed for definiteness.

On the scale of a rich cluster, a box of comoving length $L=50\,\mathrm{Mpc}$ will contain a total mass of about $9\times10^{15}\,M_\odot$. Imposing a moderate CPU ceiling of $150\,\mu$VAX hr implies that a calculation should contain $\sim10^4$ gas and $\sim10^4$ collisionless particles and take approximately 300 timesteps. Assuming a roughly isothermal cluster is grown with 1D velocity dispersion $\sigma=800\,\mathrm{km\,s^{-1}}$ ($T\simeq5\times10^7\,\mathrm{K}$), the mass contained within a radius R will be $M\sim3G^{-1}\sigma^2R=4\times10^{14}\,R\,M_\odot$. Within roughly an Abell radius $R\simeq3\,\mathrm{Mpc}$, where $M\sim10^{15}\,M_\odot$, there will be over 1000 particles of both gas and dark matter. The near galactic mass of each dark particle ($\sim10^{12}\,M_\odot$) will preclude the study of gas confined by local galactic potential wells. A bound on the gravitation softening comes from the requirement that two-body relaxation be unimportant, $GM/\varepsilon\lesssim\beta GM/R$. Using $\beta=0.05$ gives $\varepsilon\gtrsim60\,\mathrm{kpc}$. The Courant condition limit on h, using the virial sound speed and $c_2=0.3$ in equation (21), translates to a resolution limit $h_{min}\simeq150\,\mathrm{kpc}$. This size should be sufficient to resolve the cores of most X-ray emitting clusters (Sarazin 1986). Examination of cooling flows within clusters will require higher resolution.

On the galactic scale, a box of length $L=8\,\mathrm{Mpc}$ will contain $\sim4\times10^{13}\,M_\odot$. Within this volume, we would expect to find on average $1.5\,L_*$ galaxies. Each gas particle will represent $\sim4\times10^8\,M_\odot$, with the dark particles nine times as massive. So a galaxy plus dark halo system of $10^{12}\,M_\odot$ will be composed of about 300 particles of each species. We expect the rotation velocity of the haloes will be roughly $200\,\mathrm{km\,s^{-1}}$, corresponding to a virial temperature of $10^6\,\mathrm{K}$. With the same number of particle and timesteps as above, the Courant limit on h gives a value $h_{min}\sim20\,\mathrm{kpc}$. The gravitational softening limit is $\varepsilon\gtrsim6\,\mathrm{kpc}$. Better resolution could be attained by decreasing the timestep,

Table 1. Experiment resolution limits[a].

Characteristic	Galaxy	Rich Cluster
L (Mpc)	8	50
M_{tot} ($M_\odot$)	4×10^{13}	9×10^{15}
v_{vir} (km s^{-1})	200	1400
T_{vir} (K)	10^6	5×10^7
m_g ($M_\odot$)	4×10^8	9×10^{10}
m_d ($M_\odot$)	3×10^9	8×10^{11}
h_{min} (kpc)	20 (5)[b]	150
ε_{min} (kpc)	6	60
z_c	$1.6-11$	>15

[a]Estimates based on 10^4 particles for each species, timestep $\sim t_0/300\sim4.4\times10^7\,\mathrm{yr}$, and background cosmology with $\Omega_{tot}=1$, $\Omega_{gas}=0.1$, $H_0=50\,\mathrm{km\,s^{-1}\,Mpc^{-1}}$.
[b]Based on evolution up to a redshift $z=1.5$ rather than to present.

either by evolving for a shorter length of time or increasing the number of steps. For example, evolving up to a redshift $z_f=1.5$ instead of the present decreases the total evolution time, and hence increases the resolution, by a factor $(1+z_f)^{3/2}\sim 4$, bringing h_{min} down to ~ 5 kpc.

As a measure of the importance of radiative cooling processes in the calculation, we can ask when the cooling time-scale will be comparable to the expected timestep $\delta t\simeq T_H/300\simeq 4.4\times 10^7$ yr. An estimate of the cooling time is

$$t_{cool}=\frac{3kT}{n\Lambda(T)},\tag{27}$$

where $\Lambda(T)$ is the radiative cooling function. Let us evaluate the cooling for an object just collapsed at redshift z. The mean particle density within this object should be roughly,

$$n\simeq 170n_b(z)\simeq 0.9\times 10^{-4}(1+z)^3\,\text{cm}^{-3}.\tag{28}$$

For rich clusters, the dominant cooling mechanism is thermal bremsstrahlung, $\Lambda(T)= 0.6\times 10^{-23}\,T_8^{0.5}\,\text{erg cm}^{-3}\,\text{s}^{-1}$, where T_8 is the temperature in units of 10^8 K (Sarazin 1986). The ratio of cooling time to timestep is then

$$t_{cool}/\delta t\sim 4\times 10^4\,T_8^{0.5}\,(1+z)^{-3}.\tag{29}$$

For any interesting cluster temperatures, $T\sim 10^6-10^8$ K, this ratio is greater than unity unless one goes to very high redshift, $z_c\gtrsim 15$, where Compton cooling processes will be dominant anyway. Thus, cooling will not be dynamically important for the *bulk* of the mass in rich clusters.

The situation is much different on galactic scales. Approximating the primordial cooling curve of Gould & Thakur (1970) by $\Lambda(T)\sim 0.2\times 10^{-23}\,T_6^{0.6}\,\text{erg s}^{-1}\,\text{cm}^{-3}$ gives a ratio of cooling time to timestep of

$$t_{cool}/\delta t\simeq 1700\,T_6^{1.6}(1+z)^{-3}.\tag{30}$$

Choosing an isothermal temperature, $T_6=1$, gives a characteristic redshift $z_c\sim 11$ above which the expected cooling times will be shorter than the timestep. This is almost certainly an underestimate of the cooling. If we instead assume that the clustering is close to self-similar, the temperature should vary with redshift as $T\propto(1+z)^{(n-1)/(n+3)}$, where n is the effective spectral index of the initial perturbations at the scale of interest (Kaiser 1986). For $n=-2$, appropriate to the cold dark matter spectrum on galactic scales, we can write $T_6(z)=(1+z/1+z_6)^{-3}$, where z_6 is the characteristic redshift of formation for objects with virial temperature $T=10^6$ K. This leads to a very strong redshift dependence

$$t_{cool}/\delta t\simeq 1700\,(1+z_6)^{4.8}\,(1+z)^{-7.8}.\tag{31}$$

If galactic haloes are just forming today, $z_6=0$, the redshift beyond which the ratio above is less than unity is only $z_c\sim 1.6$. The situation is better for earlier formation. For example, $z_6=2.5$ gives $z_c=4.6$ and for $z_6=5.5$ we get $z_c=8.2$. The difficulties posed by such short cooling times and the implications for modelling the galaxy formation era will be examined in a later paper.

Increasing the spatial dynamic range of Courant limited calculations by a factor 2 will up the CPU time by roughly a factor $\gtrsim 16$, $\gtrsim 8$ from the number of particles and 2 from the number of timesteps. Supercomputers should easily allow room for this enhancement over the microcomputer estimates in Table 1. However, extremely wide dynamic range calculations, for example, attempting to follow the collapse of galaxies of scale 5 kpc within a larger-scale environment of order 50 Mpc, must await either a more powerful generation of computers or perhaps a more complicated, but optimized version of the general method presented here.

5 Summary

An algorithm designed to follow the hydrodynamics and thermal history of a gaseous component in 3D simulations of large-scale structure was introduced. It is the merged product of two existing particle techniques – P3M, which provides the gravity, and SPH, the hydrodynamics. The particle-based nature of the method provide a high degree of resolution for problems with complicated geometries, as will be encountered generically in simulations of cosmic structure.

Several tests of the technique were presented. Static tests showed that the kernel estimation method could reliably measure density profiles and gradients for approximately spherical systems, with only a small degree of anisotropy in the gradient. Employing variable resolution (individual h for each particle) was shown to be superior to the case of constant h. Dynamical tests of spherical systems gave good results. The region of an expanding hot gas cloud unaffected by boundary effects followed a self-similar solution through a drop in central pressure of over three orders of magnitude. The collapse and shock-heating of an initially cold gas cloud followed closely the evolution as that computed by a 1D hydro code with ~50 times the resolution. The collapse of a two-component protocluster also compared well with a similar 1D treatment. In particular, the redshift evolution of properties defined for the cluster core showed very good agreement.

Characteristic scales and resolution limits for experiments modelling rich cluster evolution and galaxy formation were briefly outlined. With 10^4 particles, runs of moderate CPU consumption on microcomputers can reach interesting resolution limits. For example, the method will be able to follow the morphological evolution of rich clusters down to scales ~150 kpc. Such a study is currently under way for clusters forming in a cold dark matter dominated universe.

Acknowledgments

References

Baron, E. & White, S. D. M., 1987. *Astrophys. J.,* **322,** 585.
Blumenthal, G. R., Faber, S. M., Primack, J. R. & Rees, M. J., 1984. *Nature,* **311,** 517.
Carlberg, R. G., 1984. *Astrophys. J.,* **286,** 416.
Carlberg, R. G., 1988. *Astrophys. J.,* in press.
Davis, M., Efstathiou, G., Frenk, C. S. & White, S. D. M., 1985. *Astrophys. J.,* **292,** 371.
Efstathiou, G. & Eastwood, J. W., 1981. *Mon. Not. R. astr. Soc.,* **194,** 503.
Efstathiou, G., Davis, M., Frenk, C. S. & White, S. D. M., 1985. *Astrophys. Suppl.,* **57,** 241.
Frenk, C. S., White, S. D. M., Efstathiou, G. & Davis, M., 1985. *Nature,* **317,** 595.
Frenk, C. S., White, S. D. M., Efstathiou, G. & Davis, M., 1987. Preprint.
Gingold, R. A. & Monaghan, J. J., 1977. *Mon. Not. R. astr. Soc.,* **181,** 375.
Gingold, R. A. & Monaghan, J. J., 1982. *Jnl Comput. Phys.,* **46,** 429.
Goldreich, P. & Weber, S. V., 1980. *Astrophy. J.,* **238,** 991.
Gould, R. J. & Thakur, R. K., 1970. *Ann. Phys.,* **61,** 351.
Gull, S. F. & Northover, K. J. E., 1975. *Mon. Not. R. astr. Soc.,* **173,** 585.
Hockney, R. W. & Eastwood, J. W., 1981. *Computer Simulation using Particles,* McGraw Hill, New York.
Kaiser, N., 1986. *Mon. Not. R. astr. Soc.,* **222,** 323.
Larson, R. B., 1969. *Mon. Not. R. astr. Soc.,* **145,** 405.
Lattanzio, J. C., Monaghan, J. J., Pongracic, H. & Schwarz, M. P., 1985. *Mon. Not. R. astr. Soc.* **215,** 125.
Lattanzio, J. C., Monaghan, J. J., Pongracic, H. & Schwarz, M. P., 1986. *SIAM J. Sci. Stat. Comput.,* **7,** 591.
Lea, S. M., 1976. *Astrophys. J.,* **203,** 569.

Loewenstein, M. & Mathews, W. G., 1986. *Jnl Comput. Phys.*, **62**, 414.
Lucy, L. B., 1977. *Astr. J.*, **82**, 1013.
McGlynn, T. A., 1984. *Astrophys J.*, **281**, 13.
Monaghan, J. J., 1985. *Comput. Phys. Rep.*, **3**, 71.
Monaghan, J. J. & Gingold, R. A., 1983. *Jnl Comput. Phys.*, **52**, 374.
Peebles, P. J. E., 1980. *The Large-Scale Structure of the Universe*, Princeton University Press, Princeton.
Peebles, P. J. E., 1982. *Astrophys. J.*, **257**, 438.
Perrenod, S. C., 1978. *Astrophys. J.*, **226**, 566.
Rees, M. J. & Ostriker, J. P., 1977. *Astrophys. J.*, **179**, 541.
Sarazin, C. L., 1986. *Rev. mod. Phys.*, **58**, 1.
Silk, J. I., 1977. *Astrophys. J.*, **211**, 638.
Thomas, P., 1987. *PhD thesis*, Cambridge University.
White, S. D. M. & Rees, M. J., 1978. *Mon. Not. R. astr. Soc.*, **183**, 341.
van Albada, T. S., 1982. *Mon. Not. R. astr. Soc.*, **201**, 939.
Yahil, A., 1983. *Astrophys. J.*, **265**, 1047.

Appendix: Details on variable h

As noted by Monaghan (1985), the use of variable h in a hydrodynamic calculation can pose difficulties for estimating gradients. The problem can be seen formally by looking at equation (11) in more detail

$$[\nabla f(\mathbf{r})]_s = \int d^3x \nabla_x f(\mathbf{x}) W[\mathbf{r}-\mathbf{x}, h(\mathbf{r}, \mathbf{x})]$$

$$= -\int d^3x f(\mathbf{x}) \nabla_x W[\mathbf{r}-\mathbf{x}, h(\mathbf{r}, \mathbf{x})], \tag{A1}$$

where the second line comes from integration by parts. The dependence of h on $\mathbf{r}$ is explicit, each particle has its own value of h which varies according to its position $\mathbf{r}$. The dependence of h on the surrounding matter at $\mathbf{x}$ comes about through the dynamic relation of h to local density – a change in the local particle distribution will cause a change in h even at constant $\mathbf{r}$. In fact, the dependence on $\mathbf{x}$ is actually stronger due to the fact that symmetric forms of the gradient (equations 13 and 14) are used between particle pairs, so that $h(\mathbf{r}, \mathbf{x})=(h(\mathbf{r})+h(\mathbf{x}))/2$ in equation (A1). Using $\mathbf{u}=\mathbf{r}-\mathbf{x}$, we can write the kernel gradient as

$$\nabla_x W(u, h) = -\frac{1}{u}\frac{\partial W}{\partial u}\mathbf{u} + \frac{\partial W}{\partial h}\nabla_x h, \tag{A2}$$

where the second term is often referred to as the 'grad-h' term. In actual practice within the code, only the first term on the right hand side is evaluated for gradient estimates. There are several ways to show that the grad-h term is, under normal circumstances, small compared to the first and can therefore safely be ignored. First, for a Gaussian kernel, the two terms above are

$$\nabla_x W(u, h) = \frac{2\mathbf{u}}{h^2} W(u, h) - \frac{3}{h}\left[1 - \frac{2}{3}\left(\frac{u^2}{h^2}\right)\right] W(u, h)\nabla_x h. \tag{A3}$$

Approximating $|\bar{\nabla}_x h| \sim h/a$, where a is the scale over which h varies appreciably, we see that the magnitude ratio of the grad-h term to the first term is

$$\frac{\text{grad-}h}{\text{grad-}u} \simeq \left[\frac{3}{2} - \left(\frac{u^2}{h^2}\right)\right]\left(\frac{h^3}{ua}\right). \tag{A4}$$

The point to note is that the dominant contribution to the hydrodynamics of any particle comes from scales $u \simeq h$. We would therefore expect that the average of $[3/2-(u/h)^2]$ is small. [In fact, for a Gaussian kernel $\int d^3u[3/2-(u/h)^2] W(u, h)=0$.] If h varies considerably on a scale $a \ll h$, then
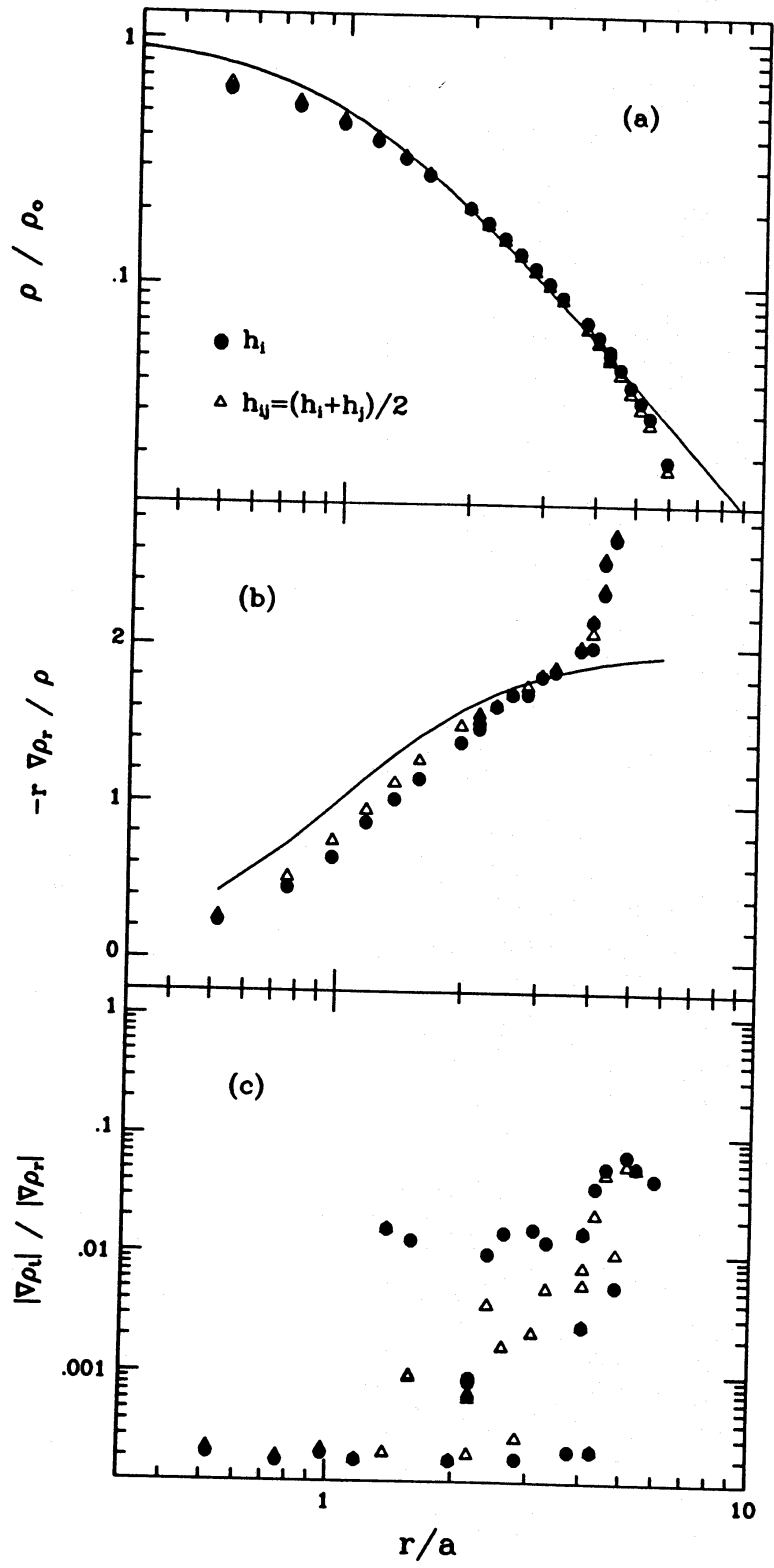
Figure A1. Re-analysis of static configuration shown in Fig. 3 using variable *h* with: (a) individual particle h_i values (solid circles) and (b) mean pairwise h_{ij} (open triangles) in sums to estimate densities and gradients (equation A5). The similarity of the two estimates indicates that particles within a distance *h* have similar smoothing lengths.

the second term may be important. In practice, it would be difficult for this situation to arise since the local density governing the size of h is always smoothed over a scale h.

A look at some particle configurations confirms the impression that grad-h terms can be safely ignored in practice. As a first example, we can consider again the static isothermal sphere of Section 3. Suppose we determine densities and density gradients in two different ways. First, we use each individual particle's h_i in Gaussian kernel sums

$$\varrho_i = \sum_j \frac{m_g}{\pi^{3/2} h_i^3} \exp\left(-r_{ij}^2/h_i^2\right), \tag{A5a}$$

$$(\bar{\nabla} \varrho_i)_r = \sum_j \frac{-2m_g}{\pi^{3/2} h_i^5} \exp\left(-r_{ij}^2/h_i^2\right) \frac{\mathbf{r}_{ij} \cdot \mathbf{r}_i}{r_i}. \tag{A5b}$$

Second, we redo the above estimates using mean pairwise h values in the above sums, i.e. $h_i \rightarrow h_{ij} = (h_i + h_j)/2$ in each of the expressions above. If h varies appreciably locally, then we would expect significant differences between the two methods of estimation. The actual results, plotted in Fig. A1, show that there is very little difference between the two procedures, indicating that particles locally have similar values of h.

As a check that this condition also holds for dynamical models, the final configuration of the two-component cosmological model of Section 3 is examined. Fig. A2 shows a scatter plot of the $(\delta h/h)_i$ plotted against local gas density. The quantity $(\delta h/h)_i$ measures the local rms variation in
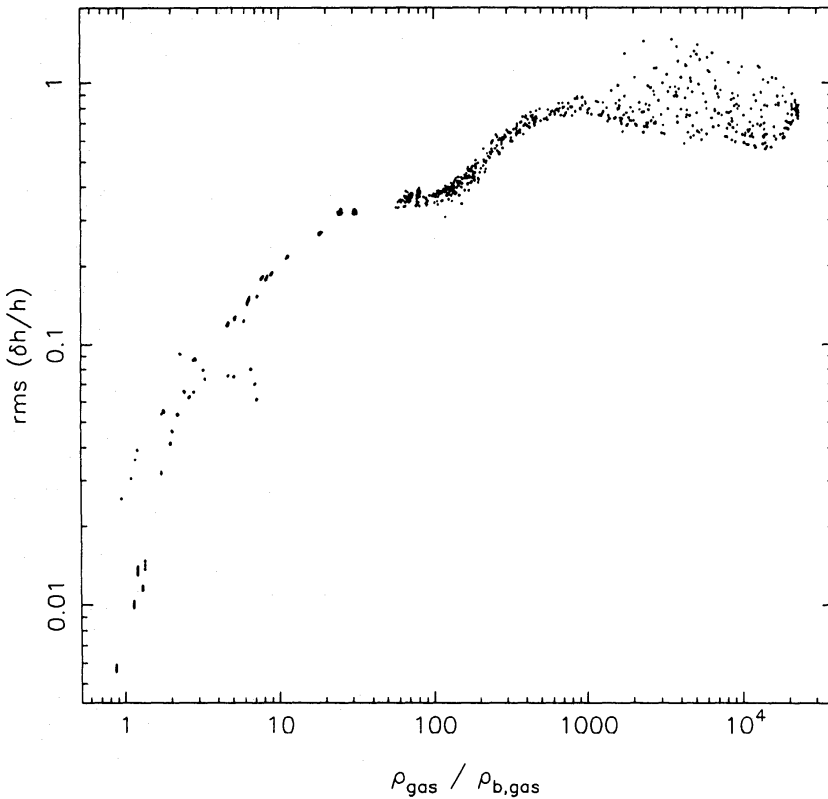

Figure A2. Local rms variation of h, defined by equation (A6), plotted against local gas density normalized to the mean background value, for the final configuration of the two-component rich cluster model of Section 3.

934   *A. E. Evrard*

h in the vicinity of particle i

$$(\delta h/h)_i = \left[m_\mathrm{g} \sum_j \frac{(h_j - h_i)^2}{\varrho_i} W(r_{ij}, h_i) \right]^{1/2} \Big/ h_i. \tag{A6}$$

It is clear from the figure that variations in h occur on roughly a scale h in the highest density regions, while below overdensities of $\sim 10^2$, the local variation in h is $\lesssim 40$ per cent. This justifies the assumption that $a \gtrsim h$ in equation (A4) above and strengthens the conclusion that, for adiabatic models, grad-h terms can safely be neglected in the gradient equations.